Research article

Carbon Future

Oxygen-tolerant CO_2 capture using protected redox-driven reverse bias bipolar membrane electrodialysis

Dawei Xi [1,3,#], Panlin Zhao [1,#], Manav Bansal [1], Olivia T. Vulpin [2], Shannon W. Boettcher [2,3] ✉, and Michael J. Aziz [1] ✉

[1] *Harvard John A. Paulson School of Engineering and Applied Sciences, Harvard University, Cambridge 02138, MA, USA*
[2] *Oregon Center for Electrochemistry, Department of Chemistry and Biochemistry, University of Oregon, Eugene, Oregon 97403, USA*
[3] *Department of Chemical & Biomolecular Engineering and Department of Chemistry, University of California, Berkeley, California 94720, USA*

Cite This: *Carbon Future* **2026**, *3*, 9200066

Read Online

ABSTRACT: Electrochemical methods for carbon capture potentially have the advantage of low cost and low energy consumption. The practical applicability of pH-swing carbon capture processes driven by proton-coupled redox-active molecules has been limited by the sensitivity of reduced molecules to oxidation by O_2. In those CO_2 capture processes, the molecules are reduced, basifying the electrolyte; the electrolyte containing the reduced molecules is exposed to air or flue gas containing CO_2 but also containing enough O_2 to oxidize the molecules. O_2 sensitivity would not be problematic if the electrolyte that captures CO_2 contains the oxidized form of the molecule instead; this can be accomplished by switching from an electron-driven system to an ion-driven system. We report the development and performance of a two-chamber flow cell incorporating a reverse-bias bipolar membrane (BPM) and non-proton-coupled redox-active molecules for ion-driven pH-swing. When using ferri/ferrocyanide electrolytes in this cell with a BPM, the cell pH can be spatially swung with the oxidized side basified for CO_2 capture and the reduced side acidified for release. Buffering agents and cell rebalancing mediators improved the efficiency and stability of the system. This work points out an alternative way of employing redox couples for electrochemically-powered pH swings.

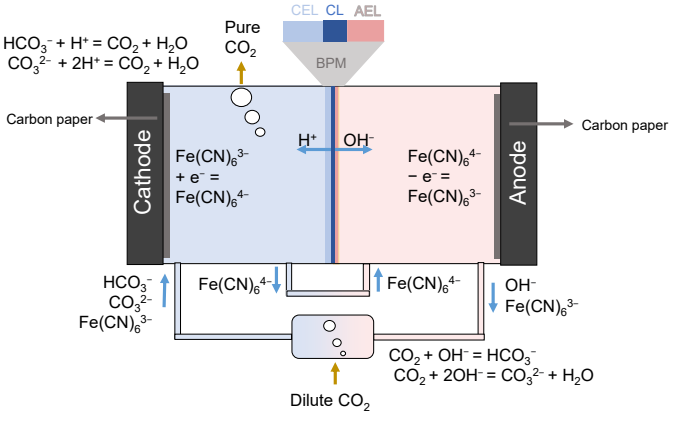

KEYWORDS: carbon capture, bipolar membrane, electrodialysis, redox mediation

1 Introduction

Effective carbon capture, utilization, and storage (CCUS)[1] technologies require chemical processes that selectively capture CO_2 from dilute streams, concentrate it, and enable permanent sequestration or conversion into stable and, ideally, valuable products[2]. Many of the chemical transformations are enabled by sequential acid-base treatments. For example, CO_2 can be captured from dilute sources as (bi)carbonate using hydroxide and subsequently released with an acid[3, 4]. Similarly, $CaCO_3$ can be converted to slaked lime ($Ca(OH)_2$) at ambient temperature through protonation to yield soluble Ca^{2+}, followed by basic precipitation[5]. Acid-base cycles are also central to the extraction and purification of metal ions from natural resources and waste streams. We note, in addition, other applications, such as the closed-circuit scrubbing of CO_2 from exhaled air during underwater diving, where O_2-tolerant reliable and regenerable systems for electrochemical CO_2 capture could be useful[6, 7].

Electrochemical methods are attractive for scaling these pH-swing transformations because they can potentially reduce energy demands relative to thermal regeneration and are more compatible with intermittent renewable electricity[8–12]. However, the redox-active molecules studied for driving a pH swing for electrochemical CO_2 capture often suffer from O_2 sensitivity, limiting practicality[13, 14].

The sensitivity to O_2 arises because the inlet gas streams that contain CO_2 typically also contain O_2[4]. For direct (**Fig. 1a**, Eqs. (1)–(6))[8, 9, 15, 16] or indirect capture[17–20] (Fig. 1b, Eqs. (7)–(12)), with step-wise (Eqs. (1)–(4) and (7)–(10)) or coupled (Eqs. (5), (6), (11), and (12)) CO_2 capture and release, to activate the electrolyte for CO_2 absorption, redox-active molecules are always reduced.

Received: October 17, 2025; **Revised:** December 10, 2025
Accepted: January 4, 2026

✉Address correspondence to Shannon W. Boettcher, boettcher@berkeley.edu; Michael J. Aziz, maziz@harvard.edu
#Dawei Xi and Panlin Zhao contributed equally to this work.

https://doi.org/10.26599/CF.2026.9200066

Upon electrochemical reduction, the increased electron density and the correspondingly raised electrolyte pH through proton absorption (pH-swing capture, a typical indirect capture) or increased molecular nucleophilicity (nucleophilicity-swing capture, a typical direct capture)[21, 22] can drive CO_2 capture from a low concentration source. However, O_2 in the feed gas can react parasitically with reduced redox molecules[4] accompanied by loss of absorption capacity and eventual cell imbalance[23]. Upon electrochemical oxidation, the electrolyte pH decreases through proton release or decreased molecular nucleophilicity, releasing the captured CO_2.

For direct capture, the thermodynamics of CO_2 binding are linked to the redox potential of the molecule: Lower redox potentials typically confer stronger CO_2 binding[23]. Efforts have therefore focused on designing molecules with more-positive redox potentials that maintain sufficient CO_2 affinity[21], separating the generated capture reagent from the redox core for indirect capture[27], or rebalancing of the cell[4]. If the redox molecule does not introduce large pH or nucleophilicity swings, an alternative strategy is to employ bipolar membranes (BPMs) to generate acid and base directly. In this case, whether the process is step-wise (Fig. 1c, Eqs. (13)–(16)) or coupled (Fig. 1d, Eqs. (17) and (18)) CO_2 absorption and release, the oxidized form of the redox molecule ends up in the higher pH electrolyte, which is used for CO_2 absorption. O_2 in air or flue gas cannot easily further oxidize the oxidized form of the redox couple, mitigating the problem of O_2 sensitivity during CO_2 capture.

The core reason for this phenomenon is that, for redox molecule-driven carbon capture systems, the charge carriers are typically non-pH-swing or non-nucleophilicity-swing ions (inactive charge carriers, such as Na^+ and Cl^-). The pH-swing or nucleophilicity-swing is introduced by the electrons injected into or extracted from the system. The systems are designed in such a way that inactive charge carriers will not cancel the pH-swing or nucleophilicity-swing the electrons bring in. Thus, those systems always drive CO_2 out (more acidic) in anolytes (when oxidized) and absorb CO_2 (more alkaline) in catholytes (when reduced). These "acidity changes" (Brønsted's pH-change or Lewis' nucleophilicity-change) are fundamentally electron-driven capture processes.

The transport of electrons and ions is always coupled[29]. When the injection or extraction of electrons does not cause pH-swing (Brønsted acid) or nucleophilicity-swing (Lewis acid) of the redox-active molecules, charge carriers that are active as Lewis/Brønsted acid and base, such as protons and hydroxide ions, can drive the release and absorption of CO_2. In this case, taking water for example, protons and hydroxides generated from water dissociation can drive pH swing in the catholyte and anolyte. As a result, ion-driven "acidity change" systems always drive CO_2 (more acidic) out of catholytes (when reduced), and absorb CO_2 (more alkaline) in anolytes (when oxidized). The relationship between pH and oxidation states is reversed by switching from electron-driven to ion-driven pH-swing.

BPMs may be utilized to generate protons and hydroxide ions as charge carriers from neutral water. BPMs are composite membranes consisting of a cation-exchange layer (CEL), an anion-exchange layer (AEL), and a catalyst layer (CL) sandwiched in between. Under reverse bias, where the CEL faces the cathode and the AEL faces the anode, BPMs drive water dissociation at their internal interface, producing protons and hydroxide ions[30, 31]. This process generates acidic and basic environments on opposite sides of the membrane and has been leveraged across diverse electrochemical applications.

To efficiently drive an ion-driven CO_2 capture system, the redox molecule should be stable over pH 6–14, non-proton-coupled, non-nucleophilicity-swing, kinetically facile, and economically accessible.

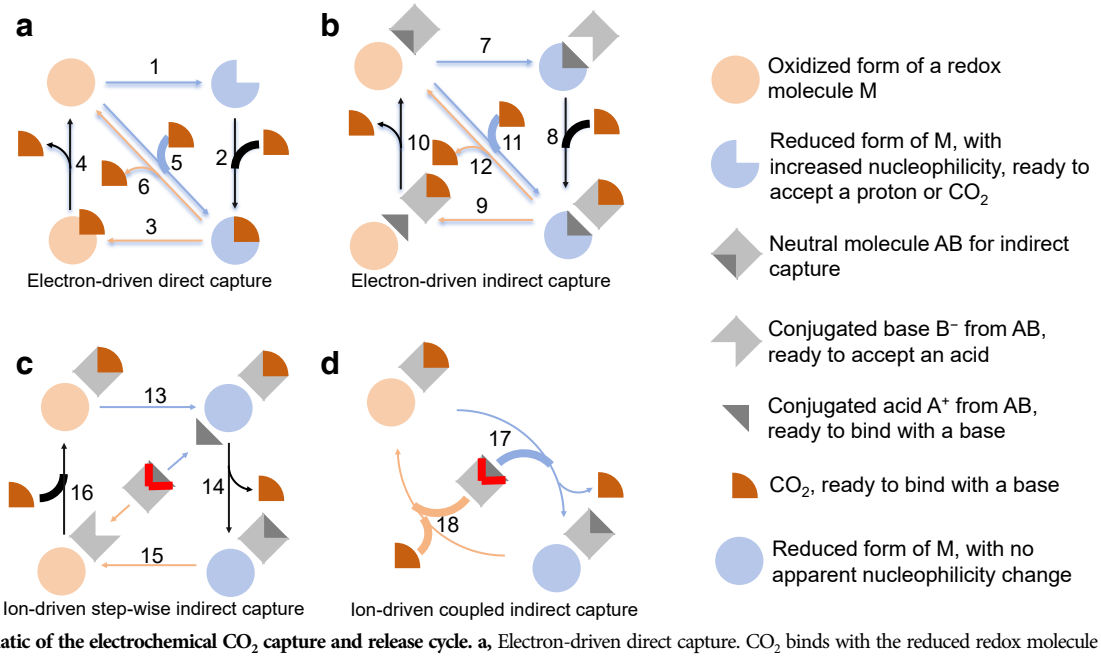

Fig. 1. Schematic of the electrochemical CO_2 capture and release cycle. a, Electron-driven direct capture. CO_2 binds with the reduced redox molecule and is released when the redox molecule is oxidized. The process can be step-wise (square process) or coupled (diagonal process). **b,** Electron-driven indirect capture. CO_2 binds with the base formed during the reduction of the redox molecule and is released when acid forms during the oxidization of the redox molecule. The process can be step-wise (square process) or coupled (diagonal process). **c,** Ion-driven indirect step-wise capture. Redox reaction of the molecule drives the dissociation of a neutral molecule, creating base in the anolyte and acid in the catholyte. **d,** Ion-driven indirect coupled capture. CO_2 binding and release can be coupled during acid/base formation.

Table 1 Reactions and examples for electron-driven direct capture

Direct capture	Electrode reaction[a]	Electrolyte reaction[b]	Charge carrier[c]	Example[d] [8, 14–16, 24]
Catholyte capture (step-wise)	(1): $M + e^- = M^-$	(2): $M^- + CO_2 = M(CO_2)^-$	Inactive ions (e.g., Li^+, Na^+, K^+, and Cl^-)	Anthraquinone (AQ) + $2e^- = AQ^{2-}$; $AQ^{2-} + 2CO_2 = AQ(CO_2)_2^{2-}$
Catholyte capture (coupled)	(5): $M + e^- + CO_2 = M(CO_2)^-$		Inactive ions	$AQ + 2e^- + 2CO_2 = AQ(CO_2)_2^{2-}$
Anolyte release (step-wise)	(3): $M(CO_2)^- - e^- = M(CO_2)^*$	(4): $M(CO_2)^* = M + CO_2$	Inactive ions	—
Anolyte release (coupled)	(6): $M(CO_2)^- - e^- = M + CO_2$		Inactive ions	$AQ(CO_2)_2^{2-} - 2e^- = AQ + 2CO_2$

[a]Electrochemical reduction and oxidation of redox molecules (M). M contributes to nucleophilicity-swing during redox reactions. Reactions are numbered as in Fig. 1a.
[b]Chemical reaction involving redox molecules (M). Reactions are numbered as in Fig. 1a.
[c]Ionic charge carriers crossing the membrane.
[d]A typical example of the reaction. AQ as M is used as an example for direct capture.

Table 2 Reactions and examples for electron-driven indirect capture

Indirect capture	Electrode reaction[a]	Electrolyte reaction	Charge carrier	Example[b] [4, 13, 17, 25, 26]
Catholyte capture (step-wise)	(7): $M + e^- + AB = MA + B^-$	(8): $B^- + CO_2 = B(CO_2)^-$	Inactive ions (e.g., Li^+, Na^+, K^+, and Cl^-)	$Pz + 2e^- + 2H_2O = H_2Pz + 2OH^-$; $2OH^- + 2CO_2 = 2HCO_3^-$
Catholyte capture (coupled)	(11): $M + e^- + AB + CO_2 = MA + B(CO_2)^-$		Inactive ions	$Pz + 2e^- + 2H_2O + 2CO_2 = H_2Pz + 2HCO_3^-$
Anolyte release (step-wise)	(9): $MA - e^- = M + A^+$	(10): $A^+ + B(CO_2)^- = AB + CO_2$	Inactive ions	$H_2Pz - 2e^- = Pz + 2H^+$; $2H^+ + 2HCO_3^- = 2H_2O + 2CO_2$
Anolyte release (coupled)	(12): $MA - e^- + B(CO_2)^- = M + AB + CO_2$		Inactive ions	$H_2Pz - 2e^- + 2HCO_3^- = Pz + 2H_2O + 2CO_2$

[a]Electrochemical reduction and oxidation of redox molecules (M). "A^+" stands for acid, and "B^-" stands for base. A^+ and B^- form neutral specie AB. For example, H_2O (AB) is constructed by H^+ (A^+) and OH^- (B^-), and $HOCH_3$ is constructed by H^+ (A^+) and OCH_3^- (B^-). Reactions are numbered as in Fig. 1b.
[b]A typical example of the reaction. Phenazine (Pz) as M in H_2O (AB) is used as an example for indirect capture.

Table 3 Reactions and examples for ion-driven capture, which can be considered as one kind of indirect capture

Ion-driven capture	Electrode reaction[a]	Electrolyte reaction	Charge carrier	Example[b] [28]
Catholyte release (step-wise)	(13): $M + e^- = M^-$	(14): $A^+ + B(CO_2)^- = AB + CO_2$	Acid A^+ from AB	$F + e^- = F^-$; $H^+ + HCO_3^- = H_2O + CO_2$
Catholyte release (coupled)	(17): $M + e^- + B(CO_2)^- + A^+ = M^- + AB + CO_2$		Acid A^+ from AB	$F + e^- + H^+ + HCO_3^- = F^- + H_2O + CO_2$
Anolyte capture (step-wise)	(15): $M^- - e^- = M$	(16): $B^- + CO_2 = B(CO_2)^-$	Base B^- from AB	$F^- - e^- = F$; $OH^- + CO_2 = HCO_3^-$
Anolyte capture (coupled)	(18): $M^- - e^- + CO_2 + B^- = M + B(CO_2)^-$		Base B^- from AB	$F^- - e^- + OH^- + CO_2 = F + HCO_3^-$

[a]Reactions are numbered as in Figs. 1c and 1d.
[b]A typical example of the reaction. Ferro/ferricyanide (F) as M in H_2O (AB) is used as an example.

In this work, we chose ferro/ferricyanide as an example of such a redox couple to drive the water dissociation with a BPM. We developed a two-chamber electrochemical flow cell that employs a reverse-biased BPM in combination with the ferri/ferrocyanide electrolyte system. Although this architecture shares some similarity to a BPM electrodialysis setup[28] for CO_2 capture from seawater, we use this work as an example to show the difference in features between electron-driven and ion-driven carbon capture systems as well as to show alternative possibilities of molecular design for carbon capture. We also introduce methods for stable operation and capacity rebalancing of such ion-driven systems. As a result, this work efficiently introduces ion-driven pH swings via charge carriers generated from water dissociation, with basified anolyte enabling CO_2 capture as carbonate and bicarbonate, followed by acidified catholyte enabling high-purity CO_2 release. However, such a system is not perfect. Therefore, we introduced buffering agents and self-rebalancing electrolytes to prevent the formation of toxic hydrogen cyanide (HCN), improving safety and stability. The system showed high efficiency at elevated current densities, demonstrating a stable oxygen-tolerant platform for continuous electrochemical CO_2 capture (**Fig. 2**). Continuous operation would require larger scale CO_2 contactors. Consequently, we operated the system in batch mode by fully oxidizing the anolyte and reducing the catholyte and manually switching the electrolytes of both sides after CO_2 capture.

2 Results and discussion

2.1 BPM-ferri/ferrocyanide electrochemical system

As a central component of the system, the bipolar membrane plays a pivotal role in determining overall system performance. Here, we systematically assessed two types of BPMs: commercially available Fumasep BPM (FBM) and a custom SnO_2-catalyzed BPM (SnO_2 BPM)[32, 33]. The custom BPM incorporates a SnO_2-nanoparticle-based catalyst layer between the cation exchange and anion exchange layers to facilitate the water dissociation reaction.

Membrane polarization using a four-electrode setup[34] indicated that SnO_2 BPM exhibited lower operating voltages (1.9 V, 200 mA·cm^{-2}) than the FBM (2.5 V, 200 mA·cm^{-2}) at the same

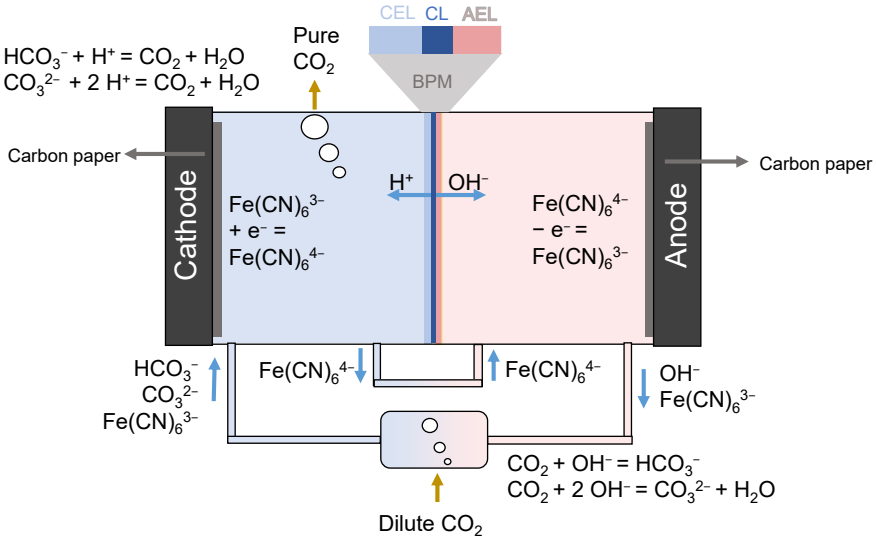

Fig. 2. Schematic of the two-chamber electrochemical acid-base generation system using a reverse-biased BPM for an ideal continuous carbon capture cycle. Such a continuous capture-release cycle requires near-complete capture before the solution is pumped into the catholyte chamber, which would require a large CO_2 contactor.

current density, primarily due to its enhanced water dissociation kinetics and ionic conductance (Supplementary Figs. S1 and S2). A further test was conducted in a 2.5 cm^2 two-chamber flow cell with BPMs separating the chambers in their reverse bias. The anolyte contained 10 mL of 0.5 M $K_4Fe(CN)_6$ and the catholyte contained 10 mL of 0.5 M $K_3Fe(CN)_6$ and 0.5 M $KHCO_3$. Constant current applied to these cells confirmed the lower voltage and energy cost under high-current-density operation with the SnO_2 BPM (**Fig. 3a**) than the FBM. However, the FBM demonstrated slightly higher current efficiency, which is defined as the experimentally measured amount of OH^- divided by the theoretical value calculated from the total charge, assuming one electron per OH^- (Fig. 3b). This difference is likely due to decreased ion recombination of salts in the FBM, caused by lower ion crossover rates through the AEL and CEL[35]. At higher current densities, the partial current contributed by ion crossover decreases, leading to enhanced current efficiency for the SnO_2 BPM (over 85% at 200 $mA{\cdot}cm^{-2}$). The lower operating voltage of SnO_2 BPM significantly improved overall energy efficiency. Energy-cost calculations showed that SnO_2 BPM required less energy to produce the same amount of OH^- than the FBM (Supplementary Fig. S3), with the current efficiency penalty considered. Specifically, at 100 $mA{\cdot}cm^{-2}$ the energy cost was 210 $kJ{\cdot}mol^{-1}$ OH^- for FBM and 130 $kJ{\cdot}mol^{-1}$ OH^- for the SnO_2 BPM, and at 200 $mA{\cdot}cm^{-2}$ the energy cost was 320 $kJ{\cdot}mol^{-1}$ OH^- for FBM and 190 $kJ{\cdot}mol^{-1}$ OH^- for the SnO_2 BPM. The possibility of operation at a high current density is important because this would allow the optimization of the levelized cost of captured carbon. A suitable current density would balance the tradeoff between operational cost (applied voltage controlled) and capital cost (current density controlled)[5]. Overall, the lower voltage operation of SnO_2 BPM reduced the system's energy consumption, making it a more energy-efficient option. The SnO_2 BPM was used for subsequent studies in this work described below.

Although ferri/ferrocyanide fits the requirement as a redox couple that does not introduce pH-swing or nucleophilicity-swing, and is stable from pH 6 to pH 14, it is not perfect due to potential HCN release when pH is lower than 6 [36]. At pH levels below 6, the increased concentration of H^+ creates conditions favorable for the protonation of ferri- and ferrocyanide species, resulting in the formation of toxic HCN. To ensure safe and efficient operation of the system, it is critical to maintain the pH above 6 throughout the cell. Ideally, the current efficiency is the same across runs, so the molarity of protons that will be injected into the catholyte during charging is identical to total alkalinity (TA, $[OH^-] + [HCO_3^-] + 2[CO_3^{2-}] - [H^+]$) of the catholyte. TA of the catholyte is generated during its previous oxidation as the anolyte before electrolyte exchange. TA of the electrolyte will not change after carbon capture (Supplementary Note S1). Thus, theoretically, in the region where the catholyte contacts the BPM, protons generated from the BPM react with hydroxide, carbonate, and bicarbonate ions in the solution, leading to only CO_2 release. However, during the cell operation, it is still possible that the local pH near the CEL side of the BPM goes lower than 6 due to the locally generated protons. A worse possible problem is that, due to the imperfect current efficiency, the amount of generated acid and base may slightly vary across runs. In those cases, once these carbonate species are depleted, the local pH may drop significantly. Therefore, it is essential to implement measures to buffer the local pH and prevent the formation of toxic gases.

To enhance system safety, histidine or sodium citrate was introduced as a local pH buffer to suppress the formation of HCN caused by ferrocyanide decomposition under acidic conditions. These buffers were selected for their suitable p*Ka* values (pKa_2 for histidine and pKa_3 for citric acid), which allow effective pH regulation above 6 without hindering CO_2 release (Figs. 3c and 3d). Experimental results confirmed that histidine successfully maintained the electrolyte pH above 6.5, preventing HCN formation, even during extended operation (Fig. 3e). In these tests, the anolyte contained 12 mL of 0.33 M $K_4Fe(CN)_6$, and the catholyte contained 12 mL of 0.33 M $K_3Fe(CN)_6$ and 0.33 M $KHCO_3$, with 0.05 M histidine or sodium citrate added as buffers. HCN formation was detected when the system was not buffered and fully charged (total molarity of generated H^+ equals the total alkalinity before charging).

To further examine HCN generation under more acidic conditions, additional ferri/ferrocyanide was introduced to increase their concentrations to 0.5 M, and the cell was continuously charged. This test simulated conditions where carbonate species

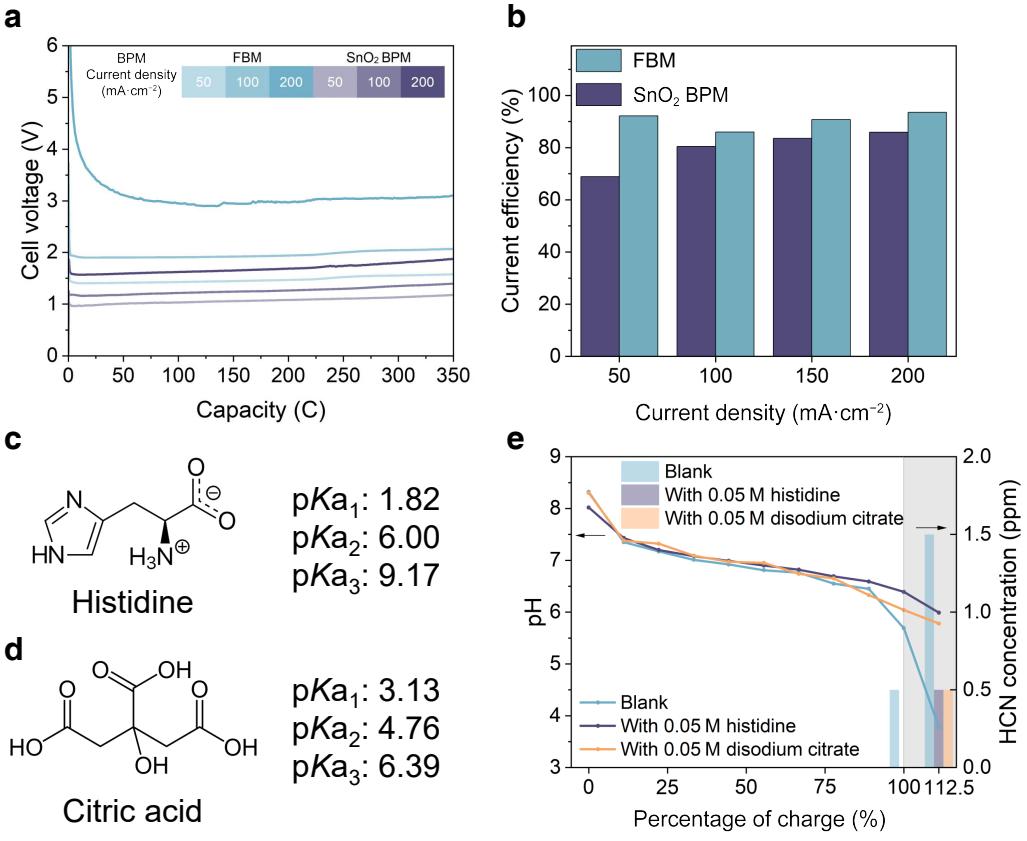

Fig. 3. Performance of the system and buffer influencing the stability of ferrocyanide. a, Voltage–capacity curves of the system under different current densities with the two selected bipolar membranes. **b,** Current efficiencies of acid-base generation of the system under different current densities with the two selected bipolar membranes. **c,** Chemical structure of histidine and its p*Ka* values. **d,** Chemical structure of citric acid and its p*Ka* values. **e,** pH variation of the catholyte and HCN concentration monitoring results of the system using the SnO_2 BPM.

were depleted or the system was over-acidified, which could be caused by SO_2 or SO_3 impurities in the inlet gas. The results showed that in the control system without the buffer, continued charging led to a significant drop in electrolyte pH below 5.7. In contrast, in the histidine- or citrate-containing system, local pH was effectively buffered, remaining above 6 when bicarbonate was depleted in the system, and no HCN gas was detected until the cell was overcharged by over 12.5%. These results demonstrate that the addition of histidine or citric acid enhanced system safety by buffering the electrolyte. We note that histidine is susceptible to be oxidized by O_2 or ferricyanide, producing 2-oxo-histidine[37], which decreases its buffer capacity. Citrate is more stable than histidine, which is advantageous for direct air capture due to its long-duration co-existence with ferricyanide at a high pH during the CO_2 capture step. For safety, pH sensors should be implemented in such systems and stop charging the cell immediately when sensing a pH lower than 6.5.

2.2 Ferricyanide reduction side reactions and system rebalancing

Although the ferrocyanide/ferricyanide redox couple remains stable against O_2 exposure during cycling, it is susceptible to reduction by side reactions under highly alkaline conditions (pH > 13.5)[36, 38]. This occurs because, in an alkaline environment, the standard electrode potential of the redox couple (~ 0.45 V vs. standard hydrogen electrode (SHE)) is more positive than the oxygen evolution reaction (OER) potential, potentially triggering the reduction of ferricyanide, accompanied by slow O_2 generation (Eqs. (19) and (20). According to previous studies[36], the presence of carbon paper significantly accelerates this reduction process, potentially due to the enhanced OER or the side reactions of carbon oxidation (Eqs. (21)–(23)).

To test this phenomenon, we monitored the concentration changes of ferricyanide solution at pH 14 using ultraviolet–visible (UV–Vis) spectrophotometry in the presence and absence of carbon paper. In the absence of carbon paper, the ferricyanide solution remained relatively stable under strong alkaline conditions (Supplementary Fig. S4). However, when carbon paper was present, the ferricyanide concentration decreased at a rate of 20% per day, confirming the occurrence of reduction by a side reaction, which affects the stability of the system.

Notably, this reduction process essentially involves the reduction of ferricyanide to ferrocyanide (Eq. 19), disrupting the redox balance of the system, pushing the electrolytes as a whole system into a more reduced state (**Fig. 4a**), with a decrease in the total alkalinity (Eqs. (22) and (23)). Based on this observation, we hypothesize that introducing O_2 that re-oxidizes the species in the electrochemical cell can eventually re-oxidize ferrocyanide back to ferricyanide, thereby restoring system capacity.

To test this approach, we selected the water-soluble anthraquinone (AQ) derivative disodium anthraquinone-2,6-disulfonate (Na_2AQDS) as a rebalancing mediator[39, 40]. When ferricyanide undergoes partial reduction by side reactions, the available charge capacity decreases (Fig. 4b, IV). By including

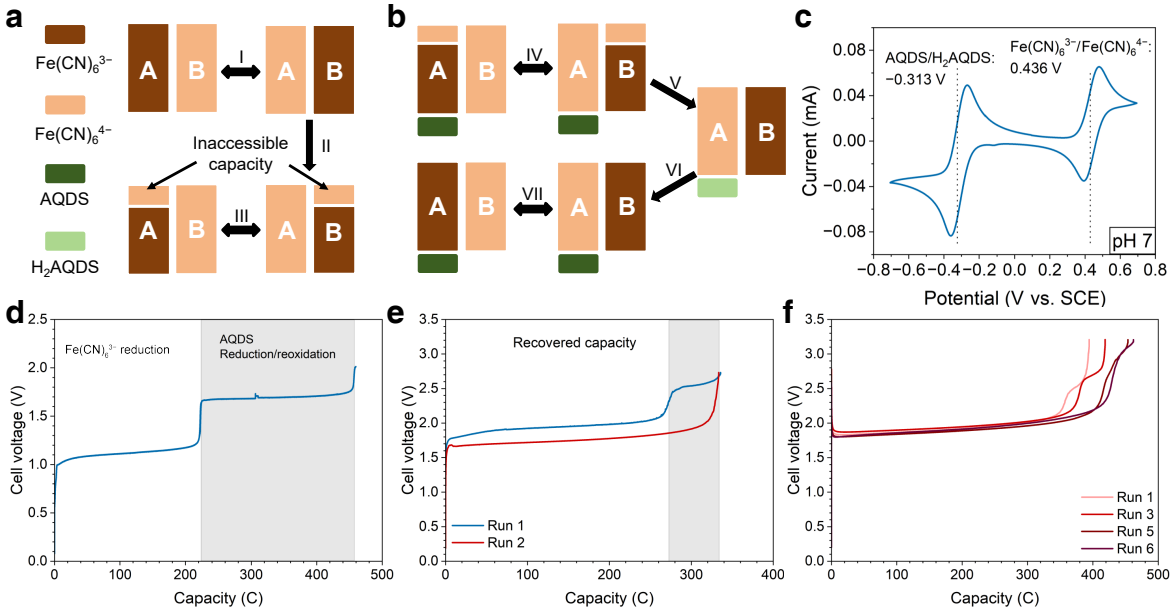

Fig. 4. Capacity rebalancing using AQDS as a rebalancing mediator. a, Schematic of cell cycling and reduction caused by side reactions. The area of the blocks indicates the concentration of redox-active molecules in the specified electrolytes A and B during cell operation. (I) Showing the change of ferro/ferricyanide concentration during cycling. (II) Showing the change of concentrations due to ferricyanide reduction caused by side reactions. (III) Showing the cycling of a capacity-imbalanced cell with inaccessible capacities. **b,** Schematic of capacity rebalancing using AQDS. (IV) Showing the change of ferro/ferricyanide concentration during cycling in a capacity imbalanced cell with rebalancing mediator AQDS. (V) Showing the potential-controlled reduction of AQDS to H_2AQDS in the catholyte accompanying the oxidation of ferrocyanide in the anolyte. (VI) Showing the oxidation of H_2AQDS to AQDS with O_2 during capacity recovery. (VII) Showing the cycling of a capacity balanced cell with AQDS in the electrolyte. **c,** Cyclic voltammograms of the ferricyanide/AQDS system at neutral pH. The difference in their redox potential allows voltage-controlled capacity rebalancing. **d,** Experimental validation of AQDS-assisted system rebalancing. Capacity rebalancing can be realized with continuous air injection into the catholyte side containing ferricyanide and AQDS at 25 $mA{\cdot}cm^{-2}$. **e,** Single rebalancing cycle at 200 $mA{\cdot}cm^{-2}$. **f,** Multi-cycle rebalancing on both sides at 200 $mA{\cdot}cm^{-2}$.

Table 4 Ferricyanide reduction by side reactions and system rebalancing reactions

	Electrode reaction	Electrolyte reaction	Net side reaction
Ferricyanide reduction and side reactions	(19): $Fe(CN)_6^{3-} + e^- = Fe(CN)_6^{4-}$	(20): $4OH^- + 4Fe(CN)_6^{3-} = O_2 + 4Fe(CN)_6^{4-} + 2H_2O$ (21): $C + 4OH^- + 4Fe(CN)_6^{3-} = CO_2 + 4Fe(CN)_6^{4-} + 2H_2O$	(22): $4OH^- - 4e^- = O_2 + 2H_2O$ (23): $C + 4OH^- - 4e^- = CO_2 + 2H_2O$
System rebalancing	(24): anode: $Fe(CN)_6^{4-} - e^- = Fe(CN)_6^{3-}$ (25): cathode: $AQDS + 2e^- + 2H_2O = H_2AQDS + 2OH^-$	(26): $2H_2AQDS + O_2 = 2AQDS + 2H_2O$	(27): $O_2 + 2H_2O = 4OH^- - 4e^-$

AQDS molecules in one side of the system, ferricyanide is first reduced in the catholyte (Eq. 24), as AQDS has a lower reduction potential (Fig. 4c). Once all ferricyanide is reduced, if any ferrocyanide in the anolyte remains partially unoxidized due to the imbalance of the cell caused by side reactions, the cell can be further charged with an increase in the charging voltage by 750 mV. At this point, AQDS in the catholyte starts to be reduced to H_2AQDS (Eq. 25), which is then oxidized by O_2, until ferrocyanide in the anolyte and AQDS in the catholyte are fully oxidized (Fig. 4b, V and VI). The oxygen in the air leads to complete rebalancing (Eq. 26, Fig. 4b, VII). This "over-charging" can restore the system's capacity by reducing oxygen into hydroxide ions as a net reaction (Eq. 27, the reverse reaction of reduction side reactions), and enables precise control over the system's reduction level through potential regulation.

To test the effectiveness of this strategy, we created intentionally misbalanced initial systems by changing the composition of the electrolyte and conducted multiple experiments, with results summarized in Figs. 4d–4f. First, to verify that AQDS can be electrochemically reduced after the depletion of ferricyanide and be chemically re-oxidized by oxygen in the air, we used 10 mL of 0.5 M $K_4Fe(CN)_6$ solution as the anolyte and 10 mL of 0.25 M $K_3Fe(CN)_6$, 0.25 M $KHCO_3$, and 0.0125 M Na_2AQDS solution as the catholyte. At a low current density of 25 $mA{\cdot}cm^{-2}$, continuous air injection into the catholyte side (Fig. 4d) demonstrated that after the depletion of the catholyte $Fe(CN)_6^{3-}$, AQDS was reduced at a higher cell voltage. The generated H_2AQDS was effectively re-oxidized by atmospheric O_2, allowing continuous charging until ferrocyanide in the anolyte was completely oxidized into ferricyanide.

We further showed that the capacity of the electrolyte can be recovered after rebalancing under a higher operational current density. We used a cell with a misbalanced electrolyte (8 mL of 0.5 M $K_4Fe(CN)_6$ solution as the anolyte and 8 mL of 0.4 M $K_3Fe(CN)_6$, 0.1 M $K_4Fe(CN)_6$, 0.4 M $KHCO_3$, and 0.05 M Na_2AQDS solution as the catholyte), then charged the cell at a

current density of 200 mA·cm^{-2} with a set voltage limit allowing the full reduction of AQDS. The charge between ferri/ferrocyanide stopped at the depletion of the catholyte $Fe(CN)_6^{3-}$ with a total of 274 C (71% of the theoretical capacity). Then, AQDS began to be reduced and started the rebalancing process, causing another charging period of 62 C. We then exchanged the electrolytes, allowing reduced AQDS to be oxidized by O_2 in air, and started a new charging process with the completion of rebalancing. The accessible capacity increased to 333 C (86% of the theoretical capacity), which is close to the sum of the previous capacity (274 C) and the recovered capacity (62 C) by AQDS (Fig. 4e). The rebalancing could be incomplete if the oxidation of H_2AQDS by air is slower than the charging rate.

Considering that in a flow system the electrolytes on both sides are continuously exchanged and hold equivalent roles, we further introduced AQDS into both electrolytes and performed simultaneous rebalancing during each cycle (Fig. 4f). Here, we used 10 mL of 0.5 M $K_4Fe(CN)_6$ and 0.025 M Na_2AQDS solution as the anolyte, and 10 mL of 0.4 M $K_3Fe(CN)_6$, 0.1 M $K_4Fe(CN)_6$, 0.4 M $KHCO_3$, and 0.025 M Na_2AQDS solution as the catholyte. We charged the cell at 200 mA·cm^{-2}, with the exchange of the electrolyte and oxidation of H_2AQDS between each charging period. The result showed that during each of the two charging periods, a portion of AQDS on each side participated in the reduction process, causing an increase in the total charge until the cell was fully balanced and eventually reaching 95% of the theoretical capacity.

2.3 Carbon capture cycle

To evaluate the system's cycling stability, particularly its adaptability to O_2 exposure, we conducted multiple cycles of CO_2 capture and release tests (**Fig. 5a** and Supplementary Fig. S5). Notably, the system was running in batch mode instead of the idealized continuous flow mode because of the limited lab-scale air contactor and electrolyte volume we used for demonstration, considering the slow kinetics of the reaction between base and CO_2.

In the anolyte, a simulated flue gas containing 15% CO_2 and 85% N_2 or 15% CO_2, 10% O_2, and 75% N_2 with a controlled 30 sccm flow rate was bubbled in as the inlet gas. The outlet gas was monitored by gas sensors to detect the concentration change of CO_2 due to absorption. In the catholyte, the released CO_2 was carried away by a stable 5 sccm pure CO_2 stream, simulating the collection of high-purity CO_2 for subsequent storage or utilization. We recorded the outlet gas flow rate to show the CO_2 release process.

The corresponding test results are shown in Figs. 5b (O_2-free conditions) and 5c (O_2-rich conditions). Here, the anolyte solution contained 10 mL of 0.4 M $K_4Fe(CN)_6$, 0.02 M Na_2AQDS, and 0.04 M histidine, and the catholyte solution contained 10 mL of 0.4 M $K_3Fe(CN)_6$, 0.4 M $KHCO_3$ (deliberately added to initiate the first cycle), 0.02 M Na_2AQDS, and 0.04 M histidine. The current density was set at 200 mA·cm^{-2}, and the maximum voltage was set at 2.0 V, which allows the full reduction of ferricyanide but no reduction of AQDS. The pH values of both catholyte and anolyte were recorded. After each cycle, the electrolytes of both sides were collected and exchanged to start the next cycle.

During charging, the cell voltage gradually increased from 1.4 to 2.0 V. Accessed capacities for each of the charging cycles were around 290 C, reaching around 75% of the theoretical capacity of 386 C (Supplementary Figs. S6–S8). Water dissociated between the layers in the BPM, and the transport of generated OH^- caused the anolyte pH to increase to ~ 13.7. Simultaneously, the CO_2 concentration in the outlet after capture through the anolyte significantly decreased, indicating absorption of CO_2. When the majority of OH^- was reacted with CO_2, the anolyte pH decreased to ~ 9. In the catholyte, the solution carrying carbonated species reacted with H^+ generated by the BPM, the pH dropped to ~ 6.2, and a distinct CO_2 release peak was detected in the pure CO_2 stream. The recorded data were very similar for each cycle, both with and without O_2 in the feed gas, demonstrating the stability of such a system for CO_2 capture and release with the presence of O_2. Sodium citrate can replace histidine as the buffer agent in such systems, and citrate is even less O_2 sensitive than histidine in the long term[37]. The generated basified electrolyte should also be capable of direct air capture and CO_2 concentration, although with a slow absorption rate.

By analyzing pH variations and gas composition data, we calculated the theoretical and actual CO_2 absorption and release amounts for each cycle (Supplementary Figs. S6–S8). The results showed that CO_2 uptake remained relatively stable and consistent over successive runs. However, due to the cell structure and the use of porous electrodes, the electrolytes on both sides cannot be completely exchanged. In addition, during the electrolyte exchange, the atmosphere in the CO_2 capture compartment temporarily changes from 15% CO_2 to air, leading to a net CO_2 release that cannot be accurately quantified by the sensor. These effects represent intrinsic limitations of the batch configuration, which cause a mismatch between the measured CO_2 absorption and release. Nevertheless, the results confirmed the system's stable operation.

In such systems, the concentration of the redox molecules matters. According to Henry's law, the difference of the amount of CO_2 dissolved in the electrolyte under low concentration CO_2 (capture gas) and pure CO_2 (release gas) will cause a "dead volume". During releasing, part of the CO_2 remains dissolved, and is released when switching to the capture gas with a lower CO_2 concentration. Theoretical calculations indicate that this thermodynamic penalty can be mitigated by increasing the concentration of the redox molecules in the electrolyte. For instance, replacing potassium ferrocyanide we use (0.40 M) with lithium ferrocyanide (solubility 2.32 M, with a solubility of lithium ferricyanide of 2.70M)[41] could reduce this "dead volume" penalty from 8.58% to 1.58%, when using 15% CO_2 as inlet gas (Supplementary Fig. S9). This effect can raise a real concern for point source capture or direct air capture when using low concentration redox electrolytes or low redox density solids to drive the capture and release.

The total energy cost for one full CO_2 capture-release cycle is 240.8 kJ·mol^{-1} CO_2 at 200 mA·cm^{-2} (Supplementary Table S1). Compared with previously reported BPM-enabled CO_2 separation systems (Supplementary Table S2), this system can operate under more than one order of magnitude higher current densities with similar energy costs, due to the lower resistance from the simplified two-chamber, single-BPM configuration. These comparisons highlight the improved operational simplicity, scalability, and full-cycle stability achieved in this work. SnO_2-BPM is relatively stable when producing acid and base[32, 33]. Adhesion between AEL and CEL can be strengthened with patterned-coated CL[42]. However, the crossover of non-proton, non-hydroxide ions can cause current efficiency loss and increased ohmic resistance.

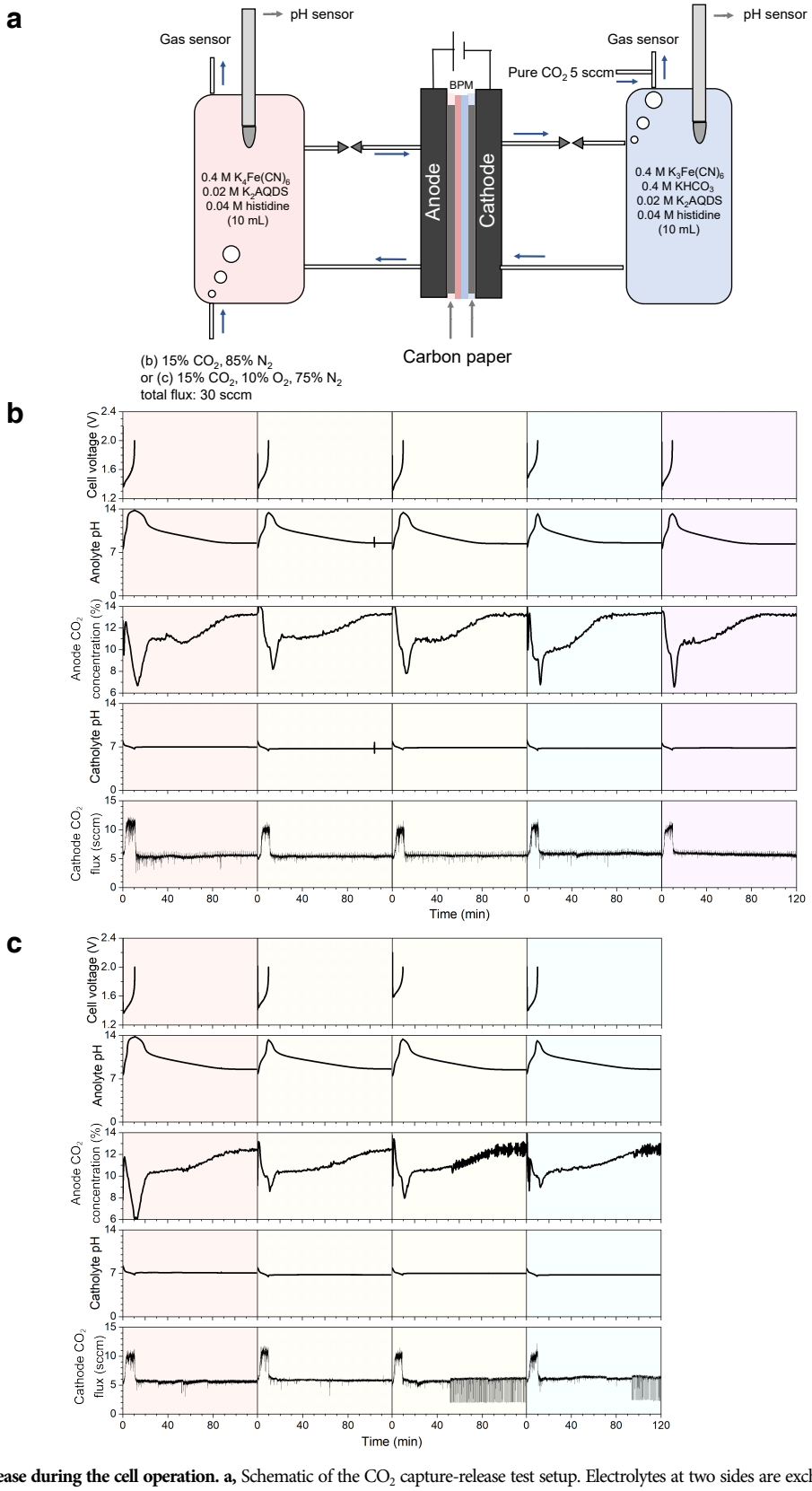

Fig. 5. CO_2 capture and release during the cell operation. a, Schematic of the CO_2 capture-release test setup. Electrolytes at two sides are exchanged between charging events. **b,** CO_2 capture and release test data under oxygen-free conditions. **c,** CO_2 capture and release test data under oxygen-rich conditions.

3 Conclusions

The utilization of a redox couple that is not proton-coupled and that does not have a large change in nucleophilicity with oxidation state, coupled with a reverse-biased BPM, reverses the typical relationship between electrochemical redox and pH swing. Whereas most electrochemical redox molecular CO_2 capture systems use electron-driven pH-swing, providing lower alkalinity with the oxidized state and higher alkalinity with the reduced state, this design is an ion-driven pH-swing process, providing higher alkalinity with the oxidized state and lower alkalinity with the reduced state. In this design, the oxidized state of the redox molecules is in contact with input gas mixtures containing CO_2 and O_2. Using this concept, the ferro/ferricyanide redox couple was used to demonstrate an efficient, oxygen-tolerant electrochemical CO_2 capture system based on reverse-biased SnO_2 BPMs. The device demonstrated ~ 90% acid and base production efficiency at high current densities (~ 200 mA·cm^{-2}) and exhibited promising operational stability. Introducing histidine or citric acids as buffering agents prevented toxic HCN formation via side reactions, enhancing safety. The use of soluble anthraquinone derivatives facilitated electrochemical rebalancing, addressing capacity decay caused by side reactions and enhancing cycling stability. In multi-cycle CO_2 capture and release tests, the system exhibited good stability and insensitivity to oxygen[42]. More generally, this study provides an alternative way of designing coupled ion-electron-transfer and redox-driven pH-swing systems and motivates the development of other non-proton-coupled and non-nucleophilicity-swing redox-active molecules.

4 Materials and methods

4.1 Materials and synthesis

Potassium ferricyanide ($K_3Fe(CN)_6$), potassium ferrocyanide ($K_4Fe(CN)_6$), potassium hydrogen phthalate, potassium bicarbonate ($KHCO_3$), histidine, acetic acid (HOAc), sodium citrate, and sodium hydroxide (NaOH) were purchased from VWR International. Na_2AQDS was obtained from TCI Chemicals. Commercial Fumasep® FAB-PK-75 bipolar membranes (FBM) were kept in distilled water before use. Carbon papers (SGL 39AA) were employed as the electrode.

Unless otherwise specified, all tests were performed in a 2.5 cm^2 zero-gap flow cell, in which a BPM was assembled in reverse bias (AEL facing anolyte, and CEL facing catholyte) between two layers of carbon paper electrodes. Electrolytes were circulated at a constant flow rate of 53 mL·min^{-1}, with the circulation volume adjusted according to the experimental configuration as specified.

All solutions were prepared using 18.2 MΩ·cm deionized water. NaOH solution for titration was prepared by dissolving 4 g of NaOH in a 500 mL volumetric flask and calibrated using potassium hydrogen phthalate. HOAc solution for titration was prepared by diluting glacial acetic acid in a 500 mL volumetric flask to obtain ~ 0.2 M HOAc. The actual concentration of the diluted HOAc solution was determined by titration against the prepared NaOH solution. Analytical-grade potassium hydrogen phthalate was used as the primary standard to calibrate the base concentration. The SnO_2 BPM was made using Nafion NR212 (50 μm, Ion Power), PiperION-A40-HCO_3 (40 μm, Versogen) and SnO_2 as the CEL, AEL, and CL, respectively. The catalyst layer SnO_2 was prepared and spray coated on top of the CEL following the reported method[32,43].

4.2 Current efficiency test

The anolyte contained 10 mL of 0.5 M $K_4Fe(CN)_6$ and the catholyte contained 10 mL of 0.5 M $K_3Fe(CN)_6$ and 0.5 M $KHCO_3$ for the current efficiency test. The cell was charged at different current densities (50, 100, 150, or 200 mA·cm^{-2}) with a capacity cutoff at 350 C. The corresponding voltage–charge profiles were recorded. After charging, 5 mL of aliquot of the anolyte was withdrawn with a micropipette and titrated with 0.2 M HOAc until the pH measured by a micro pH probe reached 7.0 to determine the amount of OH^- generated. The theoretical OH^- amount was calculated from the total charge according to Faraday's law ($n = Q/F$, assuming one electron per OH^-). The current efficiency was then obtained as the ratio of the experimentally measured OH^- amount to the theoretical value.

4.3 HCN generation test

HCN generation was evaluated with the anolyte containing 12 mL of 0.5 M $K_4Fe(CN)_6$ and the catholyte containing 12 mL of 0.5 M $K_3Fe(CN)_6$ and 0.33 M $KHCO_3$ (redox capacity: 600 C; proton buffer capacity: 400 C). A micro pH probe was immersed in the anolyte to monitor pH, and nitrogen gas was continuously bubbled through the anolyte at a flow rate of 10 mL·min^{-1} to carry any volatilized HCN into an external HCN sensor.

The cell was galvanostatically charged at 200 mA·cm^{-2} until a total charge of 450 C was passed. Charging was paused every 100 s to allow stable measurements of both pH and HCN concentration. To investigate the role of buffering, 0.05 M histidine or 0.05 M sodium citrate was added to the anolyte in separate experiments.

4.4 Cyclic voltammetry tests

Measurements were performed in a three-electrode configuration with a glassy carbon working electrode, a carbon counter electrode, and an Hg/HgO reference electrode. The electrolyte contained 0.05 M potassium ferricyanide and 0.05 M Na_2AQDS, and its pH was near neutral. Potentials were converted to the SHE scale, and the scan was conducted from −0.7 to 0.7 V (vs. SHE) at a scan rate of 50 mV·s^{-1}.

4.5 Capacity rebalancing tests

Rebalancing was evaluated under three experimental conditions. In all cases, the cells were charged galvanostatically at constant current until AQDS was completely reduced, and the corresponding voltage–charge profiles were recorded. (1) AQDS air oxidation: The anolyte contained 10 mL of 0.5 M $K_4Fe(CN)_6$, and the catholyte contained 10 mL of 0.25 M $K_3Fe(CN)_6$, 0.25 M $KHCO_3$, and 0.0125 M Na_2AQDS. Air was continuously introduced into the catholyte at 30 mL·min^{-1} during charging at 25 mA·cm^{-2}. (2) Capacity recovery: The anolyte contained 8 mL of 0.5 M $K_4Fe(CN)_6$, and the catholyte contained 8 mL of 0.4 M $K_3Fe(CN)_6$, 0.1 M $K_4Fe(CN)_6$, 0.4 M $KHCO_3$, and 0.05 M Na_2AQDS. After charging at 200 mA·cm^{-2}, the electrolytes from both chambers were collected, fully oxidized by air, and exchanged for the next charging step to evaluate the change in accessible capacity. (3) Multicycle recovery: The anolyte contained 10 mL of 0.5 M $K_4Fe(CN)_6$ and 0.025 M Na_2AQDS, and the catholyte contained 10 mL of 0.4 M $K_3Fe(CN)_6$, 0.1 M $K_4Fe(CN)_6$, 0.4 M $KHCO_3$, and 0.025 M Na_2AQDS. The cell was charged at 200 mA·cm^{-2}, and after each charging step, the electrolytes were collected, fully oxidized, and exchanged. This procedure was repeated six times to complete the capacity rebalancing.

4.6 Carbon capture tests

The anolyte contained 10 mL of 0.4 M $K_4Fe(CN)_6$, 0.02 M Na_2AQDS, and 0.04 M histidine (theoretical capacity: 384 C). A custom-built gas mixer supplied either a 15% CO_2/85% N_2 or a 15% CO_2/10% O_2/75% N_2 gas mixture as the input gas for carbon capture, which was bubbled through the anolyte at 30 mL·min^{-1}, with the outlet stream directed to a CO_2 concentration sensor. The catholyte contained 10 mL of 0.4 M $K_3Fe(CN)_6$, 0.4 M $KHCO_3$, 0.02 M Na_2AQDS, and 0.04 M histidine. Pure CO_2 was introduced into the catholyte reservoir at 5 mL·min^{-1}, and the outlet gas flow rate was monitored with a flowmeter. pH probes connected to a Gamry electrochemical workstation were placed in both the anolyte and catholyte to collect the pH of the electrolytes during operation. The cell was galvanostatically charged at 200 mA·cm^{-2} with a cutoff voltage of 2 V. After each charging process, gas flows were continued and monitored for another 120 min for carbon capture or release in the electrolyte. Afterward, the anolyte and catholyte were collected and exchanged. Each cycle thus consisted of charging until reaching the cutoff voltage, resting under gas flow, and electrolyte exchange. Voltage–charge profiles, pH values, anolyte outlet gas CO_2 concentration, and catholyte outlet gas CO_2 flow rates were continuously recorded during operation.

References

[1] Breyer, C.; Fasihi, M.; Bajamundi, C.; Creutzig, F. Direct air capture of CO_2: A key technology for ambitious climate change mitigation. *Joule* **2019**, *3*, 2053–2057.

[2] Singh, S. P.; Hao, P. J.; Liu, X.; Wei, C.; Xu, W. Q.; Wei, N.; Li, X. C.; Lu, H. R.; Ku, A. Y. Large-scale affordable CO_2 capture is possible by 2030. *Joule* **2019**, *3*, 2154–2164.

[3] House, K. Z.; Harvey, C. F.; Aziz, M. J.; Schrag, D. P. The energy penalty of post-combustion CO_2 capture & storage and its implications for retrofitting the US. installed base. *Energy Environ. Sci.* **2009**, *2*, 193–205.

[4] Jin, S. J.; Wu, M.; Jing, Y.; Gordon, R. G.; Aziz, M. J. Low energy carbon capture via electrochemically induced pH swing with electrochemical rebalancing. *Nat. Commun.* **2022**, *13*, 2140.

[5] Xi, D. W.; Yang, Z.; Emanuel, M. S.; Zhao, P. L.; Aziz, M. J. Electrochemical acid-base generators for decoupled carbon management. *Energy Environ. Sci.* **2025**, *18*, 3839–3851.

[6] Harvey, D.; Pollock, N. W.; Gant, N.; Hart, J.; Mesley, P.; Mitchell, S. J. The duration of two carbon dioxide absorbents in a closed-circuit rebreather diving system. *Diving Hyperb. Med.* **2016**, *46*, 92–97.

[7] Charnay, B. P.; Chen, Y. X.; Misleh, J. W.; Wright, J. G.; Agarwal, R. G.; Sauvé, E. R.; Toh, W. L.; Surendranath, Y.; Kanan, M. W. Membrane-free electrochemical production of acid and base solutions capable of processing ultramafic rocks. *Nat. Commun.* **2025**, *16*, 9759.

[8] Li, X.; Zhao, X. H.; Liu, Y. Y.; Hatton, T. A.; Liu, Y. Y. Redox-tunable Lewis bases for electrochemical carbon dioxide capture. *Nat. Energy* **2022**, *7*, 1065–1075.

[9] Diederichsen, K. M.; Sharifian, R.; Kang, J. S.; Liu, Y. Y.; Kim, S.; Gallant, B. M.; Vermaas, D.; Hatton, T. A. Electrochemical methods for carbon dioxide separations. *Nat. Rev. Methods Primers* **2022**, *2*, 68.

[10] Rahimi, M.; Catalini, G.; Hariharan, S.; Wang, M.; Puccini, M.; Hatton, T. A. Carbon dioxide capture using an electrochemically driven proton concentration process. *Cell Rep. Phys. Sci.* **2020**, *1*, 100033.

[11] Stern, M. C.; Simeon, F.; Herzog, H.; Hatton, T. A. Post-combustion carbon dioxide capture using electrochemically mediated amine regeneration. *Energy Environ. Sci.* **2013**, *6*, 2505–2517.

[12] Wang, M.; Herzog, H. J.; Hatton, T. A. CO_2 capture using electrochemically mediated amine regeneration. *Ind. Eng. Chem. Res.* **2020**, *59*, 7087–7096.

[13] Jin, S. J.; Wu, M.; Gordon, R. G.; Aziz, M. J.; Kwabi, D. G. pH swing cycle for CO_2 capture electrochemically driven through proton-coupled electron transfer. *Energy Environ. Sci.* **2020**, *13*, 3706–3722.

[14] Jing, Y.; Amini, K.; Xi, D. W.; Jin, S. J.; Alfaraidi, A. M.; Kerr, E. F.; Gordon, R. G.; Aziz, M. J. Electrochemically induced CO_2 capture enabled by aqueous quinone flow chemistry. *ACS Energy Lett.* **2024**, *9*, 3526–3535.

[15] Liu, Y. Y.; Ye, H. Z.; Diederichsen, K. M.; Van Voorhis, T.; Hatton, T. A. Electrochemically mediated carbon dioxide separation with quinone chemistry in salt-concentrated aqueous media. *Nat. Commun.* **2020**, *11*, 2278.

[16] Diederichsen, K. M.; Liu, Y. Y.; Ozbek, N.; Seo, H.; Hatton, T. A. Toward solvent-free continuous-flow electrochemically mediated carbon capture with high-concentration liquid quinone chemistry. *Joule* **2022**, *6*, 221–239.

[17] Pang, S.; Jin, S. J.; Yang, F. C.; Alberts, M.; Li, L.; Xi, D. W.; Gordon, R. G.; Wang, P.; Aziz, M. J.; Ji, Y. L. A phenazine-based high-capacity and high-stability electrochemical CO_2 capture cell with coupled electricity storage. *Nat. Energy* **2023**, *8*, 1126–1136.

[18] Xie, H. P.; Wu, Y. F.; Liu, T.; Wang, F. H.; Chen, B.; Liang, B. Low-energy-consumption electrochemical CO_2 capture driven by biomimetic phenazine derivatives redox medium. *Appl. Energy* **2020**, *259*, 114119.

[19] Xie, H. P.; Jiang, W. C.; Liu, T.; Wu, Y. F.; Wang, Y. F.; Chen, B.; Niu, D. W.; Liang, B. Low-energy electrochemical carbon dioxide capture based on a biological redox proton carrier. *Cell Rep. Phys. Sci.* **2020**, *1*, 100046.

[20] Jiang, W. C.; Tang, L.; Wang, Y. P.; Song, X. C.; Zhao, Z. Y.; Lan, C.; Wu, Y. F.; Liu, T.; Xie, H. P. Electrochemical proton-coupled electron transfer driven amine regeneration for CO_2 capture. *Chem. Eng. J.* **2025**, *520*, 166315.

[21] Barlow, J. M.; Clarke, L. E.; Zhang, Z. S.; Bím, D.; Ripley, K. M.; Zito, A.; Brushett, F. R.; Alexandrova, A. N.; Yang, J. Y. Molecular design of redox carriers for electrochemical CO_2 capture and concentration. *Chem. Soc. Rev.* **2022**, *51*, 8415–8433.

[22] Appel, A. M.; Yang, J. Y. Maximum and comparative efficiency calculations for integrated capture and electrochemical conversion of CO_2. *ACS Energy Lett.* **2024**, *9*, 768–770.

[23] Zito, A. M.; Clarke, L. E.; Barlow, J. M.; Bím, D.; Zhang, Z. S.; Ripley, K. M.; Li, C. J.; Kummeth, A.; Leonard, M. E.; Alexandrova, A. N. et al. Electrochemical carbon dioxide capture and concentration. *Chem. Rev.* **2023**, *123*, 8069–8098.

[24] Amini, K.; Cochard, T.; Jing, Y.; Sosa, J. D.; Xi, D. W.; Alberts, M.; Emanuel, M. S.; Kerr, E. F.; Gordon, R. G.; Aziz, M. J. *In situ* techniques for aqueous quinone-mediated electrochemical carbon capture and release. *Nat. Chem. Eng.* **2024**, *1*, 774–786.

[25] Liu, A. D.; Musgrave III, C. B.; Li, X.; Goddard III, W. A.; Liu, Y. Y. Non-aqueous alkoxide-mediated electrochemical carbon capture. *Nat. Energy* **2024**, *9*, 1415–1426.

[26] Li, X.; Musgrave III, C. B.; Liu, A. D.; Meng, J. Y.; Zhang, J. H.; Goddard III, W. A.; Liu, Y. Y. Electrifying amine carbon capture with robust redox-tunable acids. *Nat. Commun.* **2025**, *16*, 4339.

[27] Jin, X. Y.; Jin, S. J.; Li, L.; Gordon, R. G.; Wang, P.; Aziz, M. J.; Ji, Y. L. Direct air capture of CO_2 in an electrochemical hybrid flow cell with a spatially isolated phenazine electrode. *Nat. Energy* **2025**, *10*, 1146–1154.

[28] Digdaya, I. A.; Sullivan, I.; Lin, M.; Han, L. H.; Cheng, W. H.; Atwater, H. A.; Xiang, C. X. A direct coupled electrochemical system for capture and conversion of CO_2 from oceanwater. *Nat. Commun.* **2020**, *11*, 4412.

[29] Bazant, M. Z. Unified quantum theory of electrochemical kinetics by coupled ion-electron transfer. *Faraday Discuss.* **2023**, *246*, 60–124.

[30] Oener, S. Z.; Foster, M. J.; Boettcher, S. W. Accelerating water dissociation in bipolar membranes and for electrocatalysis. *Science* **2020**, *369*, 1099–1103.
[31] Chen, L. H. K.; Xu, Q. C.; Oener, S. Z.; Fabrizio, K.; Boettcher, S. W. Design principles for water dissociation catalysts in high-performance bipolar membranes. *Nat. Commun.* **2022**, *13*, 3846.
[32] Sasmal, S.; Chen, L. H. K.; Sarma, P. V.; Vulpin, O. T.; Simons, C. R.; Wells, K. M.; Spontak, R. J.; Boettcher, S. W. Materials descriptors for advanced water dissociation catalysts in bipolar membranes. *Nat. Mater.* **2024**, *23*, 1421–1427.
[33] Vulpin, O. T.; Mitchell, J. B.; Chen, L. H. K.; Lim, J.; Sasmal, S.; Price, N. G.; Jarvis, S. R.; Boettcher, S. W. Comparing advanced bipolar membranes for high-current electrodialysis and membrane electrolysis. *ACS Energy Lett.* **2025**, *10*, 845–852.
[34] Xi, D. W.; Alfaraidi, A. M.; Gao, J. X.; Cochard, T.; Faria, L. C. I.; Yang, Z.; George, T. Y.; Wang, T. B.; Gordon, R. G.; Liu, R. Y. et al. Mild pH-decoupling aqueous flow battery with practical pH recovery. *Nat. Energy* **2024**, *9*, 479–490.
[35] Bui, J. C.; Digdaya, I.; Xiang, C. X.; Bell, A. T.; Weber, A. Z. Understanding multi-ion transport mechanisms in bipolar membranes. *ACS Appl. Mater. Interfaces* **2020**, *12*, 52509–52526.
[36] Fell, E. M.; De Porcellinis, D.; Jing, Y.; Gutierrez-Venegas, V.; George, T. Y.; Gordon, R. G.; Granados-Focil, S.; Aziz, M. J. Long-term stability of ferri-/ferrocyanide as an electroactive component for redox flow battery applications: On the origin of apparent capacity fade. *J. Electrochem. Soc.* **2023**, *170*, 070525.
[37] Stadtman, E. R.; Levine, R. L. Free radical-mediated oxidation of free amino acids and amino acid residues in proteins. *Amino Acids* **2003**, *25*, 207–218.
[38] Páez, T.; Martínez-Cuezva, A.; Palma, J.; Ventosa, E. Revisiting the cycling stability of ferrocyanide in alkaline media for redox flow batteries. *J. Power Sources* **2020**, *471*, 228453.
[39] Kong, T. Y.; Liu, J.; Zhou, X.; Xu, J.; Xie, Y. H.; Chen, J. W.; Li, X. F.; Wang, Y. G. Stable operation of aqueous organic redox flow batteries in air atmosphere. *Angew. Chem. Int. Ed.* **2023**, *62*, e202214819.
[40] Huskinson, B.; Marshak, M. P.; Suh, C.; Er, S.; Gerhardt, M. R.; Galvin, C. J.; Chen, X. D.; Aspuru-Guzik, A.; Gordon, R. G.; Aziz, M. J. A metal-free organic–inorganic aqueous flow battery. *Nature* **2014**, *505*, 195–198.
[41] Li, X. T.; Yao, Y.; Liu, C. X.; Jia, X.; Jian, J. H.; Guo, B.; Lu, S. T.; Qin, W.; Wang, Q.; Wu, X. H. Lithium ferrocyanide catholyte for high-energy and low-cost aqueous redox flow batteries. *Angew. Chem. Int. Ed.* **2023**, *62*, e202304667.
[42] Kao, Y. L.; Buchauer, F.; Serhiichuk, D.; Boettcher, S. W.; Aili, D. Bipolar membranes via divergent synthesis: On the interplay between ion exchange capacity and water dissociation catalysis. *ACS Appl. Mater. Interfaces* **2024**, *16*, 58637–58647.
[43] Kao, Y. L.; Chen, L. H. K.; Boettcher, S. W.; Aili, D. Divergent synthesis of bipolar membranes combining strong interfacial adhesion and high-rate capability. *ACS Energy Lett.* **2024**, *9*, 2953–2959.

Data availability

All data needed to support the conclusions in the paper are presented in the manuscript and the Supplementary Information. Additional data related to this paper may be requested from the corresponding author upon request.

Acknowledgements

D. W. X. and M. J. A acknowledge support from the Harvard Climate Change Solution Fund and Harvard FAS Dean's Competitive Fund for Promising Scholarship. S. W. B. acknowledges support from the Office of Naval Research Award N000142512256 for work on bipolar membrane systems for CO_2 scrubbing.

Author contributions

D. W. X., P. L. Z., and M. B. designed and conducted cell tests and electrochemical experiments. O. T. V. prepared the bipolar membrane. S. W. B. and M. J. A. supervised the project. All authors drafted and edited the manuscript.

Competing interests

The authors have no competing interests to declare that are relevant to the content of this article.

Use of AI statement

During the preparation of this work, the authors used ChatGPT in order to check the grammar. After using this tool/service, the authors reviewed and edited the content as needed and take full responsibility for the content of the publication.

Additional information

Supplementary Information The online version contains supplementary material available at https://doi.org/10.26599/CF.2026.9200066.

Open Access This article is licensed under the terms of the Creative Commons Attribution 4.0 International License (http://creativecommons.org/licenses/by/4.0/), which permits use, sharing, distribution and reproduction in any medium, provided the original work is properly cited.

© The author(s) 2026. Published by Tsinghua University Press.